ELSEVIER

Journal of Alloys and Compounds 229 (1995) 24–39

Journal of ALLOYS AND COMPOUNDS

Analysis of the Verwey transition in magnetite

J. M. Honig

Department of Chemistry, Purdue University, 1393 Brown Building, West Lafayette, IN 47907-1393, USA

Received 22 December 1994

Abstract

A review is presented of work carried out in the author's laboratory concerning the thermodynamic and electrical transport phenomena in magnetite. The need for careful compositional control of single crystal growth is emphasized. With increasing deviations from the ideal Fe_3O_4 composition the Verwey transition suddenly shifts from the first order to a higher order regime. This hitherto unrecognized feature is documented by a variety of experimental techniques and is rationalized in terms of a single formalism based on a mean field theoretic approach. The agreement between theory and experiment is very good. Various aspects of the theoretical analysis are discussed in detail; the formalism is of much more general appreciability than the limited use to which it was put in the resolution of the Verwey problem.

Keywords: Verwey transition; Thermodynamics; Magnetite; Electrical transport phenomena

1. Introduction

We provide a retrospective survey concerning the Verwey transition in magnetite and describe recent developments relating to the theoretical interpretation of the results. The work is a subset of extensive measurements carried out in the author's laboratory. Emphasis will be placed in the effects of oxygen stoichiometry on the phase transition in Fe_3O_4, and on the interpretation of the experimental work. The further aim of the present paper is to illustrate procedures that are generally useful in the study of transition metal oxides. For different perspectives on this problem the reader is referred to earlier reviews [1–6].

Historically, the first indication that Fe_3O_4 exhibits a phase transition was provided by Millar in 1929 [7], who encountered an anomaly in the heat capacity near 120 K. The field remained relatively quiescent until 1939 when Verwey [8] showed that the resistivity changed discontinuously or in an anomalous manner in the 110–120 K range, depending on the mode of sample preparation. This investigation launched an avalanche of studies of the phase transformation that now bears his name: some 850 papers on this subject were published in the time interval up to 1990.

No attempt will be made to survey all of this work here. Emphasis will be placed on research of relatively recent vintage. For, it had not been properly appreciated before 1984 that careful control of sample composition is absolutely crucial for obtaining reproducible results. As a consequence there exist many contradictory claims in the earlier literature dealing with physical characteristics of magnetite above and below the transition, and about the physical changes that take place at the transition. Aside from Verwey [8] very few investigators addressed the central problem of composition control. Work before 1984 which dealt with manifestations and consequences of alterations in stoichiometry includes research by the Verwey group [8], Flood and Hill [9], Schmalzried [10], Sato [11], Kronmüller et al. [12], Dieckmann and Schmalzried [13], Kuipers and Brabers [14], Aragón and McCallister [15], and Gmelin and coworkers [16].

2. Sample preparation

As documented later, great care must be taken to prepare samples of adequate purity and homogeneity of composition in single crystal form. In earlier work problems arose through use of naturally occurring single crystals; these are always contaminated by

SSDI 0925-8388(95)01677-5

impurities in amounts sufficient to distort the findings. Where workers attempted to carry out single crystal growth from the melt they were faced with contamination by the container material, or with incorporation of carrier gases in the chemical vapor transport method. These difficulties may be avoided by employing the so-called skull melting technique described elsewhere in detail [17]. This procedure is basically a cold-crucible method: Fe_2O_3 with or without additives is placed in powdered form in a copper crucible whose base and vertical fingers are water-cooled. Powder adhering to the walls and base is kept close to room temperature; its resistance remains sufficiently high so that the material cannot couple to radio frequency powder supplied to a working coil that surrounds the crucible. However, powdered material away from the walls can be caused to couple to incident electromagnetic radiation by use of single crystals left over from a previous run, or by employing a graphite susceptor (which later burns off), buried in the powder. Either of these is elevated by the incident power to temperatures sufficiently high so as to heat contiguous powder which then also couples to the irradiation. An avalanching process ensues by which the powder is converted to a melt that ultimately reaches within several tens of microns of the crucible wall. Direct contamination is avoided by this remaining thin skull of solid material, of the same composition as the liquid. The power supply operates in the 200–400 kHz or 1–3 MHz range, depending on the size of the crucible; charges up to 2 kg in mass can be melted by operation at power levels of up to 50 kW.

Provisions must be made for control of the oxygen partial pressure so that the noncongruently melting material is maintained in the Fe_3O_4 phase field; if the pressure is too low one obtains wüstite; if it is too high the material crosses into the hematite phase region. As discussed below, the oxygen partial pressure is controlled by use of a CO/CO_2 buffer gas which circulates through a 125 L carboy. This latter cylinder also encloses a hopper through which additional starting powder is added, so as to compensate for the shrinkage in volume as the solid charge melts.

The material is maintained in the molten stage for several hours. The temperature gradients within the system produce convective stirring that facilitates equilibration with the gas; also, any dopants added to the system are uniformly dispersed. The melt is finally slowly solidified by cutting back on the power levels and lowering the crucible past the stationary work coil over several hours, using a rack and pinion mechanism. The boule is then cracked open with a hammer. Ordinarily, single crystals may be harvested from the interior in sizes ranging from 0.5 to 20 g; on one occasion a crystal weighing 60 g was obtained. The selected crystal is then oriented by X-rays and cut into the desired dimensions.

3. Annealing procedures

The above crystal growth procedure does not yield samples with a uniform oxygen/metal ratio. Accordingly, it is necessary to reanneal the specimens under a controlled atmosphere. This process is usually carried out at 1400–1450 °C where the homogeneous phase field is widest in extent, such that the cation vacancy density for $Fe_{3(1-\delta)}O_4$ is in the range $-0.0005 \leq \delta \leq 0.012$.

Equilibration is carried out in a buffering gas according to the reaction

$$CO_2 = CO + \tfrac{1}{2}O_2 \quad (1)$$

for which the equilibrium constant is given by

$$K = \frac{P_{CO}}{P_{CO_2}} P_{O_2}^{1/2} \quad (2)$$

where P are fugacities. At a fixed temperature K is fixed; the ratio of partial pressures of CO to CO_2 can be adjusted by controlling their flow rates into the reaction chamber. The partial pressure of oxygen is then determined by Eq. (2).

The dependence of δ on oxygen partial pressure is governed by the thermodynamic properties of magnetite. Here we follow the reasoning provided by Aragón and McCallister [15]. The Frenkel point disorder model applies to magnetite; even in strictly stoichiometric material there is an intrinsic concentration of cation vacancies, the displaced iron being located in interstitial positions. The generation of Frenkel defects may be depicted schematically by the 'reaction'

$$Fe = V + I \quad (3)$$

where V and I represent vacant and interstitial locations.

The associated equilibrium constant is given by

$$K_I = \frac{n_V n_I}{m_{Fe} n_\Sigma} \approx \frac{n_V n_I}{n_\Sigma^2} \quad (4)$$

where the n_i are the mole numbers of the indicated species i and n_Σ represents the total mole number of cationic species, including interstitials. For nonstoichiometric magnetite n_I and n_V necessarily differ, but Eq. (4) still holds. The generation of $Fe_{3-d}O_4$ by oxidation proceeds via two distinct mechanisms: the first is the incorporation of excess oxygen onto regular anionic sublattice sites; since the number of iron ions remains fixed, oxygen addition generates cation vacancies that distribute themselves uniformly by diffusion. Formally, (ie. for strictly bookkeeping purposes)

one can assign to each oxygen ion a charge of −2; electroneutrality requires the conversion of two Fe^{2+} ions to two Fe^{3+} ions when excess oxygen is incorporated. The process may be schematically represented by the 'reaction'

$$Fe^{2+} + \tfrac{1}{4}O_2 = Fe^{3+} + \tfrac{1}{2}O^{-2} + \tfrac{3}{8}V \quad (5)$$

in conformity with the Fe_3O_4 stoichiometry of magnetite. The corresponding equilibrium constant is (O^{-2} represents an anion lattice site)

$$K_V = \frac{n_{3+}}{n_{2+}}\left[\frac{n_V}{n_\Sigma}\right]^{3/8} P_{O_2}^{-(1/4)} \quad (6)$$

A second oxidation mechanism involves the diminution in concentration of interstitial cations. This process is represented by the 'reaction'

$$Fe^{2+} + \tfrac{1}{4}O_2 + \tfrac{3}{8}I = Fe^{3+} + \tfrac{1}{2}O^{-2} \quad (7)$$

with a corresponding equilibrium constant given by

$$K_I = \frac{n_{3+}}{n_{2+}}\left[\frac{n_\Sigma}{n_I}\right]^{3/8} P_{O_2}^{-(1/4)} \quad (8)$$

From considerations involving mass and charge balance one may represent $Fe_{3-d}O_4$ as $(Fe^{3+})[Fe^{2+}_{1-3d}, Fe^{3+}_{1+2d}]O_4$, where the round and square brackets represent iron in tetrahedral (t) and octahedral (o) coordination. Consistent with experimental observation [18], t sites are occupied exclusively by Fe^{3+}, whereas o sites contain both di- and trivalent iron, as well as cation vacancies. The above relation shows that per unit cell there exist 2(1 + d) trivalent and (1 − 3d) divalent iron ions. It is then trivial to establish that $n_{3+} - 2n_{2+} = 8d$, so that the mole fraction of cation vacancies is given by $\delta \equiv d/n_\Sigma$, where δ is the parameter in the general formula unit $Fe_{3(1-\delta)}O_4$ for nonstoichiometric magnetite. Using the relation

$$(n_{3+} + n_{2+} + n_V)/n_\Sigma = 1 \quad (9)$$

and the expression

$$\delta = \frac{1}{8}\left(\frac{n_{3+} - 2n_{2+}}{n_\Sigma}\right) \quad (10)$$

one may solve for

$$\frac{n_{3+}}{n_\Sigma} = 8\delta + 2\frac{n_{2+}}{n_\Sigma}; \qquad \frac{n_{2+}}{n_\Sigma} = \frac{1}{3}\left(1 - 8\delta - \frac{n_V}{n_\Sigma}\right) \quad (11)$$

One may also eliminate n_I in terms of n_V and δ from Eqs. (4), (10), and (11). This yields

$$(n_V/n_\Sigma)^2 - \delta(n_V/n_\Sigma) - K_I = 0 \quad (12)$$

The positive root of the quadratic solution may now be substituted in Eq. (11) to yield

$$\frac{n_{3+}}{n_{2+}} = 2 + [(24\delta)/(1 - 8\delta - \delta/2 - \sqrt{\delta^2/4 + K_I})] \quad (13)$$

and when this and the positive root of Eq. (12) is introduced in Eq. (6) one obtains

$$P_{O_2}^{1/4} = \frac{1}{K_V} \times\left\{2 + \left[(24\delta)\Big/\left(1 - 8\delta - \left(\frac{\delta}{2} + \frac{1}{2}\sqrt{\delta^2 + 4K_I}\right)\right)\right]\right\} \times\left(\frac{\delta}{2} + \frac{1}{2}\sqrt{\delta^2 + K_I}\right)^{3/8} \quad (14)$$

The equilibrium parameters K_V and K_I have been determined through meticulous gravimetric measurements by Dieckmann and Schmalzried [13]; the temperature variation of these parameters is given by

$$K_V = \frac{4456}{T} - 2.64 \quad (15)$$

and

$$K_I = -\frac{10740}{T} - 1.23 \quad (16)$$

On substituting Eq. (15) and (16) into (14) one can determine the oxygen fugacity in equilibrium with magnetite of composition $Fe_{3(1-\delta)}O_4$ as a function of temperature.

The variation of $\log P_{O_2}$ vs. $1000/T$ is shown in Fig. 1 for various $\delta = d/3$ in the phase field. The outermost lines correspond to the phase boundaries for the hematite-magnetite and wüstite-magnetite phase fields.

Annealed samples with large δ values that are cooled slowly will ultimately cross the stability phase boundary; the resulting exsolution process produces

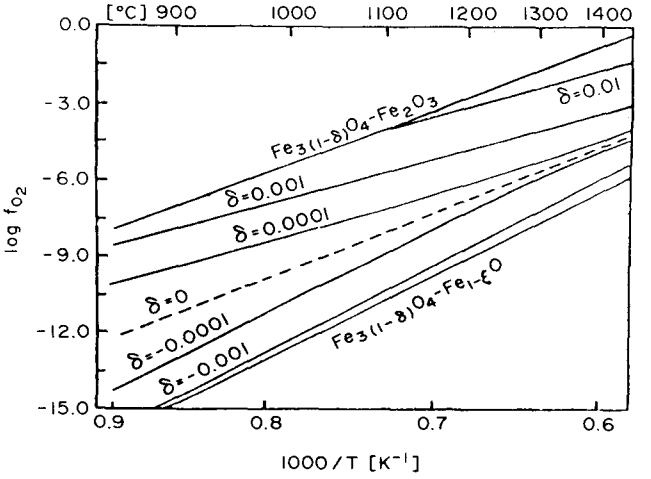

Fig. 1. Phase field for $Fe_{3(1-\delta)}O_4$ as determined by thermogravimetric analysis; after Ref. [15]. Heavy lines designate equilibrium phase boundaries. At the low pressures prevailing here, $f_{O_2} \equiv P_{O_2}$.

two-phase mixtures at low temperature. To avoid this problem samples with large δ must be quenched and cannot be reheated to temperatures at which equilibration resumes on a short time scale.

As mentioned earlier, the desired P_{O_2} is achieved by circulation of appropriate CO/CO_2 mixtures over the sample. However, one cannot rely on the rather crude control mechanism provided by flowmeter readings. Accordingly, an oxygen transfer cell is used, with Y_2O_3-stabilized ZrO_2 as the 'electrolyte.' Oxygen gas in one compartment is circulated past the electrodes at one atmosphere, and gases in equilibrium with the sample flow through the second compartment placed adjacent to the sample. The EMF of this Nernst concentration cell is given by

$$E = \frac{RT}{4F} \ln P_{O_2} \tag{17}$$

where R is the gas constant, F the Faraday, and P_{O_2} is the equilibrium oxygen pressure to be established, which can thus be monitored by EMF measurements. Details concerning the above annealing procedures may be found in several publications, [15,17,19].

It remains to establish the annealing times required to ensure uniformity of sample composition. This is dictated by the rate of diffusion of cation vacancies through the lattice. From careful tracer diffusion experiments [13] the diffusion coefficient was found to vary with temperature as

$$D_V = 0.143 \exp\left[\frac{-137 \text{ kJ mol}^{-1}}{RT}\right] \quad (\text{in cm}^2\,\text{s}^{-1}) \tag{18}$$

The relevant equation governing diffusion is Fick's second law, $j = -D_V \nabla c$, where j is the diffusion current density and ∇c is the gradient of the the vacancy concentration. For a semi-infinite slab of thickness $2a$ the limiting solution obtained from the diffusion equation is given by [20]

$$\frac{c(x) - c_0}{c_1 - c_0} = 1 - \frac{4}{\pi} \exp\left[\frac{-\pi^2 D_V t}{4a^2}\right] \tag{19}$$

where $c(x)$ is the final concentration profile at position $-a \leqslant x \leqslant a$, c_0 is the initial concentration, and c_1 the concentration at the outer boundaries.

Calculated concentration profiles are shown in Fig. 2, where the curve labels represent $D_V t^2/a$ values. A flat concentration profile is attained for $D_V t^2/a \geqslant 1.5$, which provides an estimate of the time t required to achieve uniformity of composition. For instance, the appropriate time span at 1000 °C is 3–306 h for samples of thickness of 1–10 mm; at 1400 °C the corresponding values are 2 min–14 h. Once equilibration is complete the sample must be rapidly brought to room temperature.

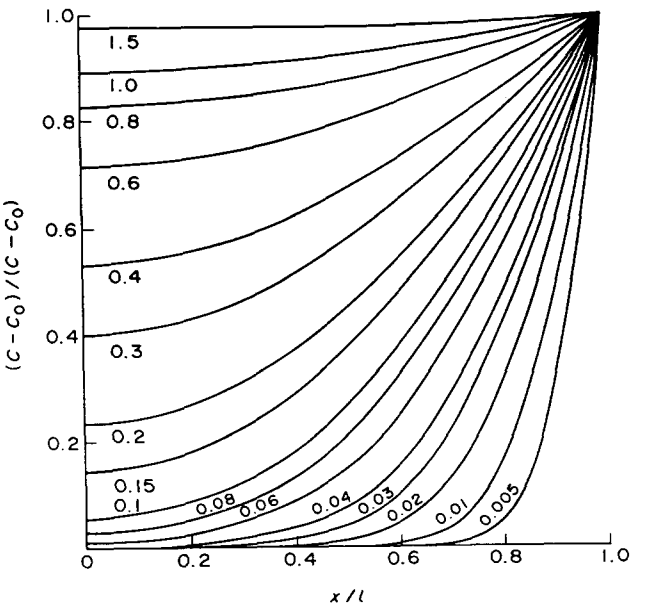

Fig. 2. Diffusion profiles for attainment of equilibrium in a semi-infinite slab of thickness $l = 2a$. See text for elaboration.

Unfortunately, no matter how fast the material is quenched the outer portions are altered in composition even during rapid cooldown to below 600 °C. Therefore, the outer surfaces of the single crystal specimens were always trimmed off until a central core of uniform composition was obtained.

4. Heat capacity measurements

The need for careful control of sample composition becomes evident on examining the history of heat capacity measurements that dates back to 1929. The diversity of findings are reviewed in several articles [1,2,21] and need not be reexamined, being of historic interest only.

Results reported by Shepherd et al. [21] are reproduced in Figs. 3 and 4. These authors were the first to report a rather unusual occurrence, namely a change in the nature of the phase transition with increasing departures from the ideal 4/3 ratio of oxygen/iron. In the composition range $-0.0005 < \delta < 0.0039 \equiv \delta_c$, (Group I samples) $Fe_{3(1-\delta)}O_4$ exhibits a first order phase transition. This is documented by the heat capacity anomaly in the form of a spike at the Verwey temperature T_V. It is further verified by the thermal arrest in the heating and cooling curves when the sample temperature is moved past T_V—indicative of a latent heat of transition. A typical curve is reproduced in Fig. 5; the corresponding ΔH_V can be calculated from the area under the arrest; one should note the temperature scale on the ordinate. The

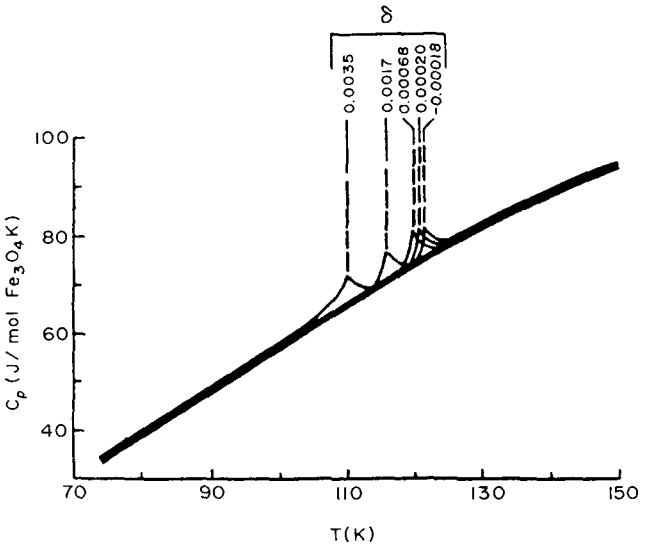

Fig. 3. Heat capacity vs. temperature for $Fe_{3(1-\delta)}O_4$ samples in the first order transition regime $-0.0005 < \delta < \delta_c = 0.0039$; after Ref. [21].

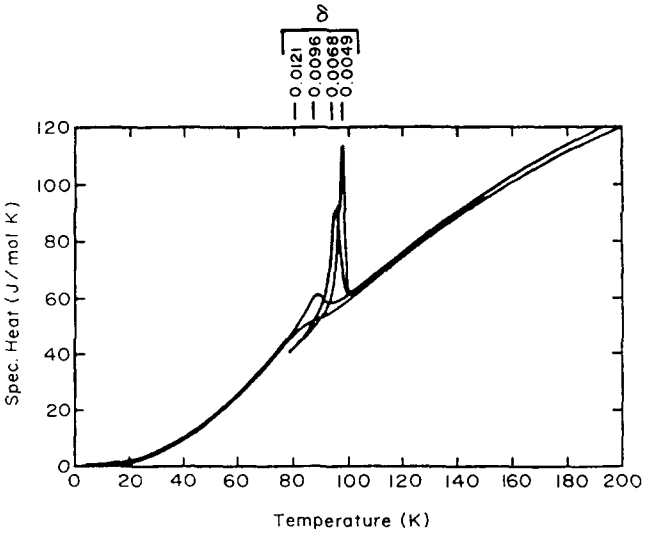

Fig. 4. Heat capacity vs. temperature for $Fe_{3(1-\delta)}O_4$ samples in the higher order transition regime $\delta_c < \delta < 3\delta_c$; after Ref. [21].

corresponding entropy of the phase change is obtained as $\Delta S_V = \Delta H_V / T_V$.

In the range $\delta_c < \delta < 3\delta_c$ the material undergoes a higher order transition, probably of second order (Group II samples): the heat capacity peak is now very broad and has roughly a Λ-type shape with a maximum at T_V. Also, no thermal arrest is encountered in the heating and cooling cycles.

The composition range $\delta > 3\delta_c$ is not accessible because one reaches the magnetite–hematite phase boundary just beyond $\delta = 3\delta_c$. However, resistivity data taken on the closely related zinc ferrites

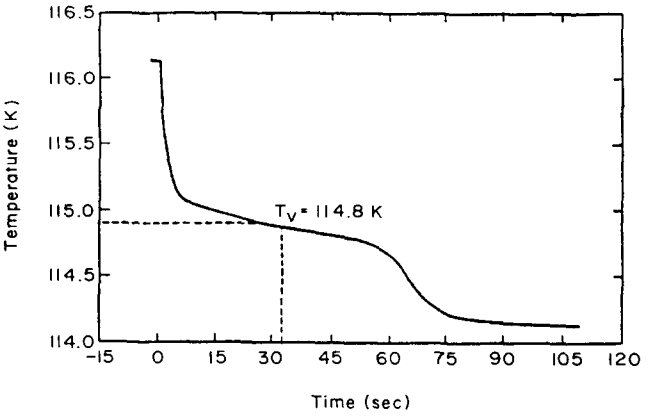

Fig. 5. Cooling curve for $Fe_{3(1-\delta)}O_4$ with $\delta = 0.0017$ near the Verwey transition. Note temperature scale and thermal arrest.

$Fe_{3-x}Zn_xO_4$ and titanomagnetites $Fe_{3-y}Ti_yO_4$ [24] suggest that the transition would disappear entirely if samples with composition $\delta > 3\delta_c$ could be stabilized.

That second order samples differ thermodynamically from those in group I is documented in Fig. 6. The difference in the heat capacities of Group I vs. Group II specimens is maintained down to the lowest attained temperature of 0.3 K [22]. The Debye temperatures of the two sets are in the range $\Theta_I = 539 \pm 47$ K and $\Theta_{II} = 511 + 24$ K respectively.

Several other points are noteworthy. First, there is a linear variation of T_V with δ; the data taken from heat capacity and electrical (see below) measurements are entered as circles in Fig. 7. One readily discerns the two regimes that characterize the phase transition: for category I the transitions occur in the range $122\ \text{K} > T_V > 108\ \text{K}$; for category II the corresponding range is $101\ \text{K} > T_V > 83\ \text{K}$. Second, all samples exhibit virtually the same variation of C_p with T for $T > 124$ K, despite the C_p differences between samples at lower

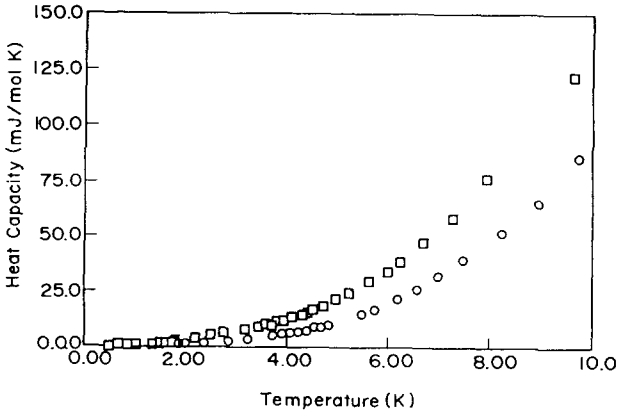

Fig. 6. Low-temperature heat capacity curves for $Fe_{3(1-\delta)}O_4$. Upper curve $\delta = 0.0049$ (higher order sample); lower curve $\delta = 0$ (first order sample).

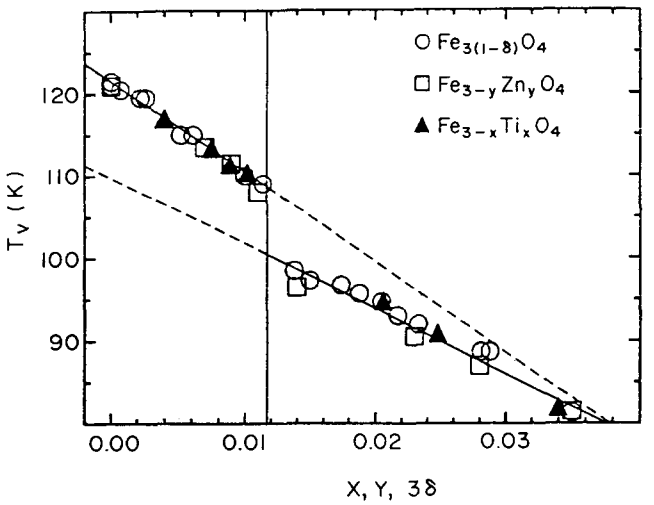

Fig. 7. Variation of the Verwey transition temperature T_V with composition of $Fe_{3(1-\delta)}O_4$, $Fe_{3-x}Zn_xO_4$, $Fe_{3-y}Ti_yO_4$. Circles are based on heat capacity and electrical measurements taken on magnetite.

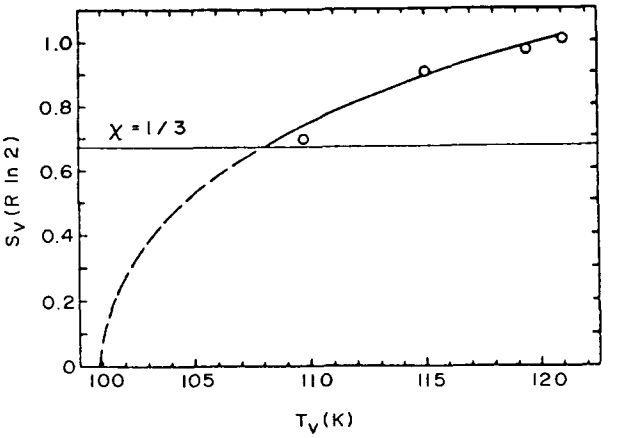

Fig. 8. Change of entropy of transition of nonstoichiometric magnetite in category I as a function of T_V. Open circles: experimental data; solid curve: theoretical analysis. See text for details.

temperatures. Thus, it is only in the low temperature phases of magnetite that differences in C_p are encountered. Third, there are small pre- and post-monitory effects present in the first order transitions. Their origin is presently unclear, but they may be related to lattice relaxation effects that occur immediately above and below the sharp first order transition. Fourth, the critical δ value marking the boundary between the two groups of samples has been estimated at $\delta_c = 0.0039$. This figure may be rationalized as follows: for a unit cell in the low temperature configuration the total number of cations is $n_\Sigma = 96$. When one divalent ion is oxidized to the trivalent state one finds that $n_{3+} - 2n_{2+} = 3$. When used in the expression $\delta = (8n_\Sigma)^{-1}(n_{3+} - 2n_{2+})$ one obtains $\delta_c = 3/8n_\Sigma = 0.0039$. Thus, the order of the transition changes precisely at the point where the symmetry of each unit cell has been disrupted through the conversion of one out of 96 cations from the ferrous to the ferric state.

We next turn to the measured entropies ΔS_V of the transition; detailed listings have been provided in the literature [21,25]. ΔS_V varies from 6.0 ± 0.1 to 4.0 ± 0.1 J mol^{-1} K over the range $-0.0002 \leq \delta \leq 0.0035$; these data are entered as open circles in Fig. 8; the curve will be discussed at a later stage. For Group II materials the entropy must be estimated from the area under the heat capacity anomalies shown in Fig. 4. The precision of the results is severely compromised by the problems of accurately estimating the baseline. ΔS_V values fall in the range 1.78–1.08 J mol^{-1} K—these remain well below those of Group I samples. Of great interest is the value of $\Delta S_V = R \ln 2 = 5.91$ J mol^{-1} K for the first order transition in stoichiometric magnetite, instead of $\Delta S_V = 2R \ln 2$, which had generally been cited. Any theory purporting to interpret the nature of the transition must explain not only the change in order of the transition but also this apparent anomaly.

5. Electrical measurements

A second technique for investigating the Verwey transition is electrical resistivity and Seebeck coefficient measurements. The results are shown in Figs. 9(a) and 9(b).

Care was taken to ensure that problems arising from anomalous conduction through surface layers were eliminated. All resistivity (ρ) measurements were carried out by a four-probe technique on oriented crystal specimens. Probes were attached to samples using silver paste; temperatures were measured via calibrated carbon glass thermometers. Seebeck coefficient (α) measurements were executed by slowly changing the temperature of one end of the sample relative to the other while continuously monitoring the corresponding voltage drops; α was determined from the slope of the curve obtained by plotting more than 1000 data points after establishing a temperature differential of 1 K. The procedure was repeated roughly 225 times in the range 75–300 K.

Examination of Fig. 9(a) immediately reveals a difference in electrical properties of Group I vs. Group II samples. At T_V there is a discontinuity of resistivity or a discontinuity in its temperature derivative respectively. Above T_V all samples exhibit virtually the same variation in resistivity with temperature. Consistent with heat capacity data, one encounters a drop in T_V with increasing departures from ideal stoichiometry (increasing δ), as well as a drop in the size of the resistivity anomaly. The hysteresis in the

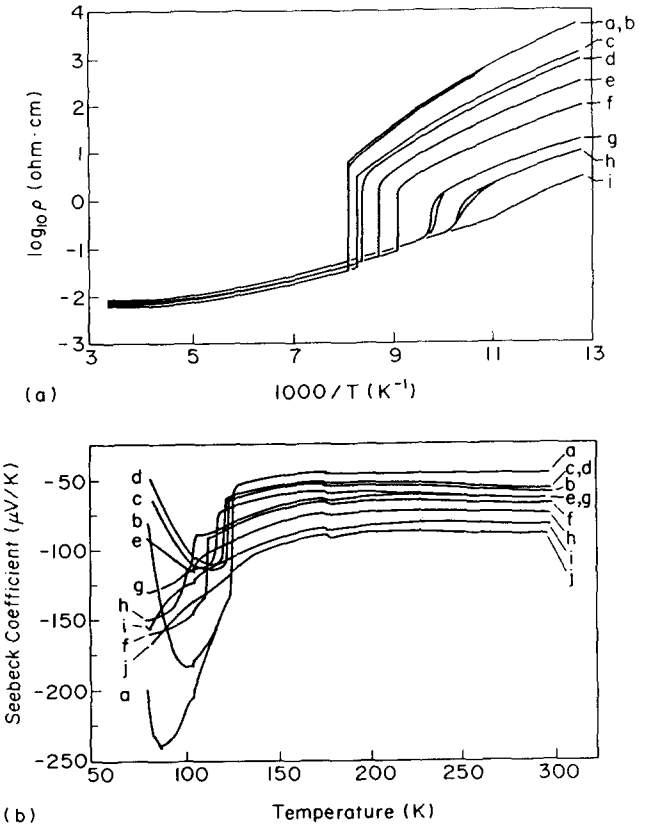

Fig. 9. (a) Resistivity (ρ) of $Fe_{3(1-\delta)}O_4$ as a function of temperature for various compositions, plotted as log ρ vs. $1/T$. Note discontinuity in ρ at T_V for samples in Group I and discontinuity in $d\rho/dT$ at T_V for samples in Group II. (b) Seebeck coefficient (α) of $Fe_{3(1-\delta)}O_4$ as a function of temperature for various compositions, plotted as α vs. T. Note discontinuity in α at T_V for samples in Group I and discontinuity in $d\alpha/dT$ at T_V for samples in Group II. The upturn in α at low temperatures is spurious.

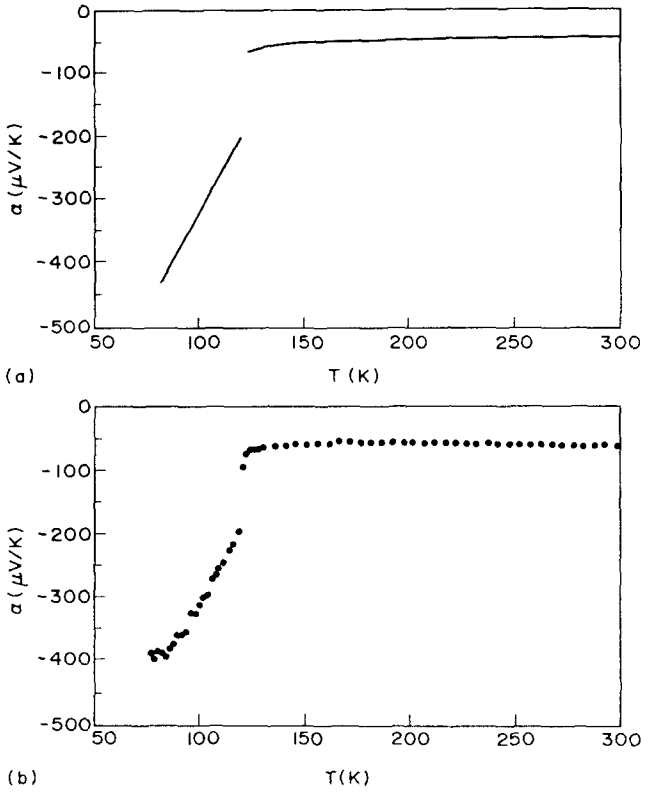

Fig. 10. Seebeck coefficient measurements on highly pure stoichiometric magnetite as a function of temperature. Part (a) solid curve: calculated Seebeck coefficients. Part (b), points: experimental data.

first order transition is of the order of 0.3 K, again consistent with heat capacity measurements. In Group II specimens the temperature coefficient of resistivity is discontinuous. The much larger hysteresis loop in resistivity for Group II samples has recently been correlated [25a] with similar observations of structural changes as one proceeds past the Verwey transition temperature. This reflects the existence of small ordered domains in a background of disorder; the overall structural characteristics depend on whether the material is heated or cooled. Note further then the plots in Fig. 9(a) are not linear; also, the phase transitions at T_V are not actually metal–insulator transformations; instead, one encounters a change in semiconducting characteristics. This matter is discussed more fully below.

Corresponding features are found in the thermoelectric measurements. At T_V there is a discontinuity of α for Group I samples and discontinuity of $\partial\alpha/\partial T$ for Group II specimens. For $T > T_V$ all magnetite samples display almost constant α values that become more negative as δ increases. Below T_V α first becomes more negative with decreasing temperature and then increases at still lower T values. A very similar trend was reported in earlier work by Kuipers and Brabers [14]. This particular low-temperature feature can be greatly altered or entirely eliminated by working with very high purity samples and with specimens subjected to an applied magnetic field [26]. In such circumstances the increase in $-\alpha$ with decreasing T is almost linear down to the lowest measured temperatures, as shown in Fig. 10(b).

6. The Strässler–Kittel Model

The above experiments clearly document that even small changes in oxygen stoichiometry drastically affect the course of the Verwey transition. We have attempted to find a single theoretical model for rationalizing the above results. The exposition provided below proceeds in several stages.

A minimalist approach was furnished by Strässler and Kittel [27] (SK) on the basis of a two-state model, with energies $E_0 \equiv 0$ and E_1, and degeneracies g_0 and g_1, and with a population distribution n_0 and n_1 respectively. They introduced a single order parameter

$\psi \equiv n_1/N$ where $N \equiv n_0 + n_1$. The number of independent ways of distributing n_1 subsystems among N sites is given by

$$W = g_0^{N-n_1} g_1^{n_1} \frac{N!}{(N-n_1)!n_1!} \tag{20}$$

The Boltzmann entropy is given by $S = k_B \ln W$; then, for sufficiently large n_1 one obtains in Stirling's approximation

$$S(\psi) = k_B N[\psi \ln g_1 + (1-\psi)\ln g_0 - \psi \ln \psi - (1-\psi)\ln(1-\psi)] \tag{21}$$

where the last two terms are the conventional entropies of mixing of two states, and the first two arise from the ad hoc introduction of degeneracies.

The energy of the interacting particle assembly was specified by SK as

$$U(\psi) = N(\epsilon\psi - \tfrac{1}{2}\lambda\psi^2) \tag{22}$$

which is a two-parameter expression. The term in ϵ specifies the energy for $N\psi$ independent particles residing at energies ϵ above the ground state, and the second term mimics the interaction between particles ($\lambda > 0$). The difference in energy on promoting a particle from the ground to the excited state is given by

$$U(n_1+1) - U(n_1) = \epsilon - \lambda\psi - \lambda\psi/2N \approx \epsilon - \lambda\psi \equiv \bar{U} = \partial U/\partial n_1 \tag{23}$$

This is, as expected, the partial molal internal energy characterizing the system.

One can now construct the Helmholtz free energy as

$$F/N = [U(\psi) - TS(\psi)]/N = \epsilon\psi - \tfrac{1}{2}\lambda\psi^2 - k_B T[\psi \ln g_1 + (1-\psi)\ln g_0 - (1-\psi)\ln(1-\psi) - \psi\ln\psi] \tag{24}$$

where one must require that $\epsilon \geq \lambda/2 > 0$ in order to guarantee that $\psi = 0$ at $T = 0$.

Equilibrium constraints are imposed by demanding that $\partial(F/N)/\partial\psi = 0$; this yields the so-called equation of state, derived by SK:

$$\epsilon - \lambda\psi - k_B T\left[\ln\left(\frac{g_1}{g_0}\right) + \ln\left(\frac{1-\psi}{\psi}\right)\right] = 0 \tag{25}$$

As discussed below, the variation of ψ with T is strongly affected by the choice of the parameters ϵ, λ, and g_1/g_0. This equation seems to be the only one proposed so far that can deal with different types of transitions.

(a) For first order changes one requires that there exist two specific, symmetrically placed values $0 < \psi_1 < 0.5$ and $0.5 < \psi_2 < 1$, such that $F(\psi_1) = F(\psi_2)$, $F'(\psi_1) = F'(\psi_2) = 0$, $F''(\psi_1)$, $F''(\psi_2) > 0$. Eq. (24) can be broken down into a contribution F_{sym} symmetric in the interchange $\psi \to 1-\psi$, and into a contribution F_l linear in ψ. Recognizing the symmetry, we introduce a variable $0 \leq \kappa \leq 1$, such that

$$\psi_1 = \frac{1-\kappa}{2}, \qquad \psi_2 = \frac{1+\kappa}{2} \tag{26}$$

Following Kloor [25] we may set

$$F/N = a\psi + b\psi^2 + F_{sym}/N \tag{27}$$

with $a \equiv \epsilon - k_B T \ln(g_1/g_0)$, $b \equiv -\lambda/2$, and F_{sym} given by the remaining terms in Eq. (24). Substituting Eqs. (26) and (27) into the relation $F(\psi_1) = F(\psi_2)$ with $T = T_V$ we obtain

$$2a(1-\kappa) + b(1-\kappa)^2 = 2a(1+\kappa) + b(1+\kappa)^2 \tag{28}$$

which reduces to

$$\epsilon - \lambda/2 = k_B T_V \ln(g_1/g_0) \tag{29}$$

One can now define a reduced Verwey temperature by

$$x_c \equiv k_B T_V/\lambda = (\epsilon/\lambda - \tfrac{1}{2})[\ln(g_1/g_0)]^{-1} \tag{30}$$

A general analysis shows that $F(\psi)$ must be at a maximum at $\psi = 0.5$, so that $F''(0.5) < 0$. After differentiating Eq. (25) with respect to ψ, and setting $T = T_V$ in the inequality we find $k_B T_V/\lambda < 1/4$. On now introducing the right hand side of Eq. (29) and the constraint $\epsilon \geq \lambda/2 > 0$, we obtain

$$\frac{1}{2} \leq \frac{\epsilon}{\lambda} < \frac{1}{2} + \frac{1}{4}\ln\left(\frac{g_1}{g_0}\right) \tag{31}$$

which shows that $g_1 > g_0$ is a necessary (though not sufficient) condition for a first order transition to take place.

Additionally, Strässler and Kittel distinguish between a super first order (S) or normal first order (N) transition according as $\psi(T > T_c) > \psi_\infty$ or $\psi(T > T_V) < \psi_\infty$, where ψ_∞ is the order parameter at infinite temperature. As is seen from Eq. (25), for $1/T = 0$,

$$\psi_\infty = \frac{g_1}{g_1 + g_0} \tag{32}$$

From Eq. (25) it follows that an S or N transition occurs for $\epsilon/\lambda - \psi_\infty < 0$ or $\epsilon/\lambda - \psi_\infty > 0$ respectively; alternatively, $\bar{U} < 0$ and $\bar{U} > 0$ respectively.

A typical plot of the order parameter ψ vs. reduced temperature $k_B T/\lambda$ is shown in Fig. 11(a); this will be discussed more extensively below.

(b) A second order transition is characterized by a critical value ψ_c such that the first three derivatives of F with respect to ψ vanish at ψ_c and the fourth derivative at ψ_c is positive. From Eq. (24) and from the requirement that $F'''(\psi_c) = 0$ we find $k_B T[(1-\psi_c)^{-2} - \psi_c^{-2}] = 0$, which can hold only if $\psi_c = 1 - \psi_c$, whence $\psi_c = 0.5$. From $F''(\psi_c) = 0$ one obtains $\lambda = k_B T_c/\psi_c(1-\psi_c)$, which for $\psi_c = 0.5$ means that $\lambda = 4k_B T_c$. The requirement $F''''(\psi_c) > 0$ translates into

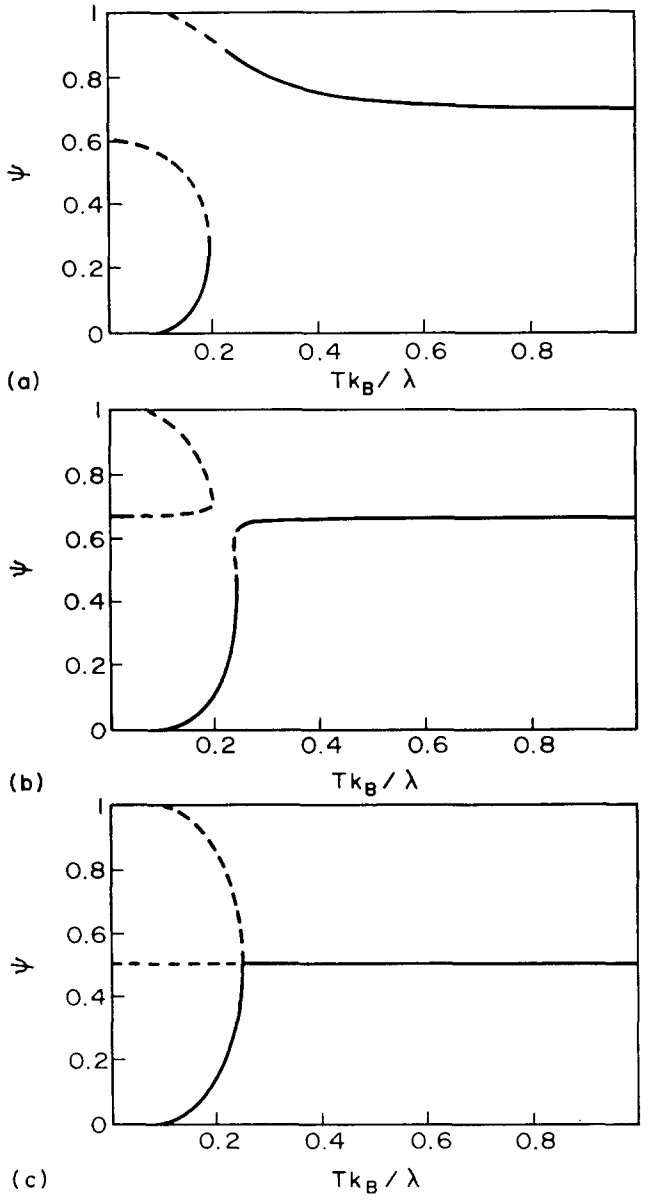

Fig. 11. Plot of order parameter ψ vs. reduced temperature $k_B T/\lambda$. Part (a): $\epsilon/\lambda = 0.60$, $g_1/g_0 = 2$; part (b): $\epsilon/\lambda = 2/3$, $g_1/g_0 = 2$; part (c): $\epsilon/\lambda = 1/2$, $g_1/g_0 = 1$. Dashed portions indicate physically unrealizable solutions to Eq. (25). After Ref. [25].

$k_B T[\psi_c^3 + (1-\psi_c)^3]\ (\psi_c - \psi_c^2)^{-3} > 0$, which, together with $F'(\psi_c) = 0$, $\psi_c = 0.5$ and $\lambda = 4k_B T_c$ leads to

$$\frac{\epsilon}{\lambda} = \frac{1}{2}\left(1 + \frac{1}{2}\ln\left(\frac{g_1}{g_0}\right)\right) \tag{33}$$

One sees that only for ϵ/λ values satisfying Eq. (33) does a second order transition occur; additionally, the requirement $\lambda = 4k_b T_c$ must be met. This can be done by setting $\lambda = 2\epsilon$ and $g_1 = g_0$, so that $\epsilon = \lambda/2 = 2k_B T_c$. It is very important to note that the equation of state for the second order transition is also given by Eq. (25), but in the present case $g_1 = g_0$ so that $\epsilon - \lambda\psi - k_B T \ln[(1-\psi)/\psi] = 0$ is the resulting relation.

(c) Lastly we consider the case $g_1 < g_0$, in conjunction with the requirement $\epsilon/\lambda \geq 1/2 > 0$. We see that for $g_1/g_0 < 1$ one cannot then satisfy either the right hand side of Eq. (31) or Eq. (33). Thus, first or higher order transitions are ruled out for $g_1 < g_0$.

The mathematical arguments presented above are verified by numerical calculations involving the equation of state. Typical results are shown in Fig. 11 for a variety of ϵ/λ values as plots of ψ vs. $k_B T/\lambda \equiv x$. The dotted curves represent parts of the solution that are not physically realizable. Note that in Fig. 11(a) we set $\epsilon/\lambda = 0.60$ and $g_1/g_0 = 2$; there is a discontinuity in ψ at $k_B T/\lambda = 0.2$, characteristic of first order transitions. The latter is of type S: with rising T_V, ψ diminishes towards $\psi_\infty = 2/3$ for $k_B T/\lambda > 0.2$. Fig. 11(b) represents a case where $\epsilon/\lambda = 2/3$ and $g_1/g_0 = 2$. Here one encounters a mix of a second order transition terminated by a discontinuity, as documented by the presence of loops in the diagram; these must be treated by the conventional equal area rule. The existence of such a case was recognized for the first time by Kloor [25]. Lastly, we note that for $\epsilon/\lambda = 0.5$ and $g_1/g_0 = 1$ the plot shown in Fig. 11(c) indicates that ψ is continuous at $k_B T/\lambda = 0.2$ but the slope of the curve is discontinuous at that point. This situation is characteristic of a second order transition.

Kloor [25] has argued that ψ reflects both the global, long range order and the local order, and that the latter prevails primarily above the Verwey transition. This is consistent with the post-monitory effects encountered for Group I samples in the heat capacity measurements above T_V. It is likewise consistent with the marked high temperature tail of the Λ-type anomaly seen in heat capacity measurements of Group II specimens.

7. The Hijmans-de Boer Order–Disorder Model

The SK formulation treats the various manifestations of the Verwey transition within a single framework but does not provide a connection between the two-state system of Strässler and Kittel and the properties of magnetite. To address this problem Honig, Spałek, and Gopalan [28] injected the basic concepts of order–disorder theory into the model, with the very limited objective of 'deriving' the SK equation of state, Eq. (25). This also required placing Eq. (24), which had been presented by SK on a very ad hoc basis, on a firmer footing. Honig and Spałek [28] directed attention to the important role played by octahedral site pairs. Since the tetrahedrally coordinated cationic sites contain only Fe^{3+} ions, valence fluctuations of these cations seem very unlikely. By

contrast, the octahedrally coordinated sites contain both Fe^{3+} and Fe^{2+}, consistent with valence fluctuations. One may regard the $Fe^{3+}d^5$ cores as 'vacuum states;' the Fe^{2+} ions are generated by the extra electrons shared among o-coordinated cations. These can respond to externally applied electric fields and to temperature changes. The lowest energy state is realized at $T = 0$ when Fe^{2+} ions are surrounded solely by Fe^{3+} ions and vice versa; the 'extra' electrons are then as far removed from each other as possible. On the other hand, this is also the state of lowest entropy, so that at $T > 0$ the state of the system is determined by a balance between these two opposing tendencies, i.e. through minimization of the free energy. This requires consideration of states where the extra electrons occupy neighboring o-sites.

In lowest approximation one might therefore mock up magnetite by a collection of independent octahedral site pairs. Three sets of possible occupation states are listed in Table 1 and depicted schematically in Fig. 12.

The lowest energy state shown in Fig. 12(a), is one in which the single electron is localized at one of the two sites on the octahedrally coordinated site pair; a concomitant lattice distortion occurs simultaneously around any such site C occupied by the electron; A, the other member of the site pair, is empty. The CA configuration mimics the low-temperature lattice distortion; the corresponding AC possibility is excluded, since its presence would set up a cancelling lattice distortion in the opposite direction. An electron in the ground state C cannot respond to an applied electric field. A first excited state is generated by promoting an electron to an undistorted o-site where it has access to either member of the o-site pair with equal probability. The promoted electron is represented by state B; this configuration is depicted in Fig. 12(b). Clearly the resonant BA and AB configurations are precursors to the directed drift of electrons in an applied electric field, and thus represent the conducting states. Lastly, there is a state of highest energy, Fig. 12(c), in which two electrons occupy adjacent o sites, giving rise to a BB configuration. Such carriers cannot move toward each other but may proceed to adjacent empty sites and are therefore itinerant.

Table 1
Lattice Representation

Configurations	Probability		Energy
	Bond representation		
● ●	BB	β_2	ϵ_{BB}
● ○	BA	$2\beta_1$	ϵ_{BA}
○ ●	AB		ϵ_{AB}
⊗ ○	CA	β_0	ϵ_{CA}
	Site representations		
●	B	γ_2	ϵ_2
○	A	γ_1	ϵ_1
⊗	C	γ_0	ϵ_0

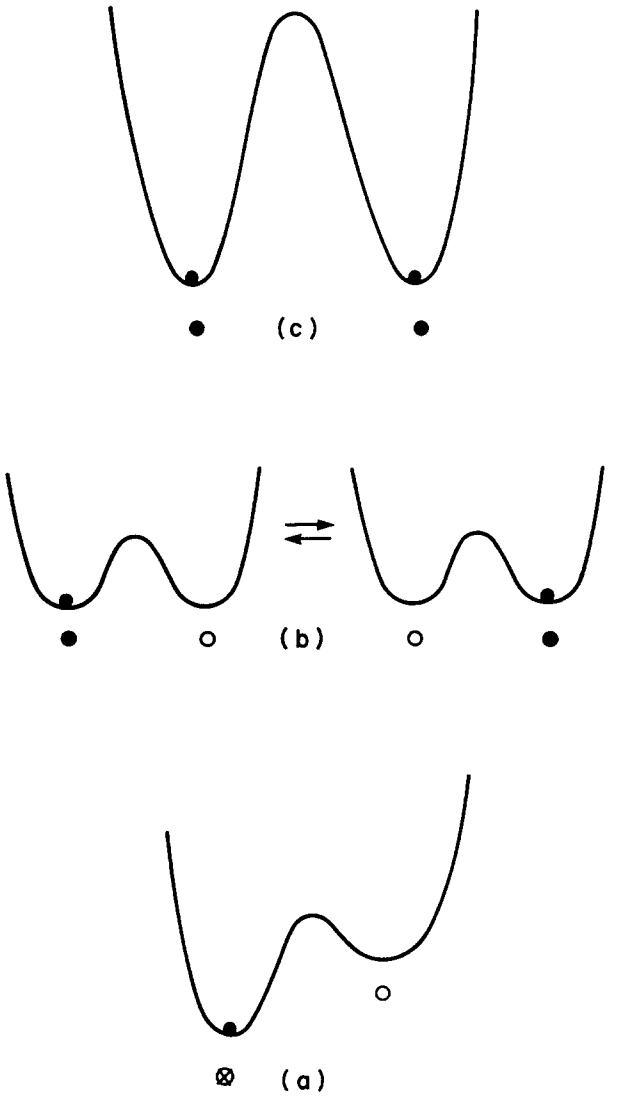

Fig. 12. Schematic representation of bond occupation states listed in Table 1. For explanation see text.

Once the configurations have been specified the remainder of the derivation is straightforward. One distinguishes between sites C, A, and B which are assigned the occupation probabilities γ_0, γ_1, and γ_2 respectively, as shown in Table 1; the corresponding energies are designated ϵ_0, ϵ_1, and ϵ_2 respectively. The CA, BA and AB, and BB configurations shown in Table 1 are assigned probabilities β_0, β_1, β_1, and β_2 respectively. These variables are not independent: first one must take account of the normalization conditions

$$\beta_2 + 2\beta_1 + \beta_0 = 1 \tag{34a}$$

$$\gamma_2 + \gamma_1 + \gamma_0 = 1 \tag{34b}$$

Second, the quantity γ_1 is fixed by the sample

composition $Fe_{3(1-\delta)}O_4$; for $\delta = 0$, $\gamma_1 = 0.5$. Lastly, we adopt the consistency condition for mobile carriers: the bond representation for a lattice of N sites contains $(Z/2)N$ members, where Z is the number of nearest neighbors to any given site; the factor 0.5 prevents overcounting of pairs. These $ZN/2$ bonds already include ZN individual sites, whereas the correct count is only N. Hence one must introduce a corrective set of $(1-Z)N$ units as a site assembly, so that the total number of sites in the two lattice representations properly tallies to N.

Examination of Table 1 shows that the total number of mobile carriers in the bond and site representations is $(Z/2)N(2\beta_1 + 2\beta_2)$ and $(1-Z)N\gamma_2$ respectively, compared with $N\gamma_2$ carriers in the lattice proper. To match the tallies one must therefore thirdly require that

$$\beta_1 + \beta_2 = \gamma_2 \tag{34c}$$

which is known as a consistency condition.

The above constrains reduce the number of independent variables from six to two; we shall select β_1 and γ_2 as the independent set. We also rewrite Eqs. (34a)–(34c) as

$$\beta_2 = \gamma_2 - \beta_1 \qquad \beta_0 = 1 - \gamma_2 - \beta_1 \qquad \gamma_0 = 1 - \gamma_2 - \gamma_1 \tag{35}$$

It is now a simple matter to construct the energy of the bond figure assembly from Table 1 as

$$\begin{aligned} E_b &= (Z/2)N(\beta_2\epsilon_{BB} + 2\beta_1\epsilon_{AB} + \beta_0\epsilon_{CA}) \\ &= (Z/2)N(\beta_2 U + 2\beta_1 E + \epsilon_{CA}) \end{aligned} \tag{36}$$

where we have set $U \equiv \epsilon_{BB} - \epsilon_{CA} = U(\beta_2)$, $E \equiv \epsilon_{AB} - \epsilon_{CA} = E(\beta_1)$.

Note that U and E depend on β_2 and β_1 respectively; this degree of freedom is essential to take proper account of the shift in energies that occurs when electrons on neighboring sites are allowed to interact.

The energy of the site assembly is similarly given by

$$\begin{aligned} E_s &= (1-Z)N(\gamma_2\epsilon_2 + \gamma_1\epsilon_1 + \gamma_0\epsilon_0) \\ &= (1-Z)N(\gamma_2\epsilon_B + \gamma_1\epsilon_A + \epsilon_0) \end{aligned} \tag{37}$$

where $\epsilon_B \equiv \epsilon_2 - \epsilon_0$, $\epsilon_A \equiv \epsilon_1 - \epsilon_0$.

In Stirling's approximation the entropy of the bond figure assembly is given by

$$S_b = -k_B(Z/2)N(\beta_2 \ln \beta_2 + 2\beta_1 \ln \beta_1 + \beta_0 \ln \beta_0) \tag{38}$$

and that of the site figure assembly is

$$S_s = -k_B(1-Z)N(\gamma_2 \ln \gamma_2 + \gamma_1 \ln \gamma_1 + \gamma_0 \ln \gamma_0) \tag{39}$$

One can then construct a Helmholtz free energy function:

$$F = E_b + E_s - T(S_b + S_s) = F(\gamma_2, \beta_1) \tag{40}$$

and optimize the resultant by imposing the equilibrium constraints $(\partial F/\partial\gamma_2) = (\partial F/\partial\beta_1) = 0$. On collecting Eqs. (36)–(40) and imposing the latter constraint one obtains

$$\begin{aligned} 0 = \frac{Z}{2}N\left[\beta_2 U'\left(\frac{\partial\beta_2}{\partial\beta_1}\right) + U\left(\frac{\partial\beta_2}{\partial\beta_1}\right) + 2E + 2\beta_1 E'\right] \\ + k_B T\frac{Z}{2}N\left[\left(\frac{\partial\beta_2}{\partial\beta_1}\right)\ln\beta_2 + \left(\frac{\partial\beta_2}{\partial\beta_1}\right) + 2\ln\beta + 2 \right. \\ \left. + \left(\frac{\partial\beta_0}{\partial\beta_1}\right)\ln\beta_0 + \frac{\partial\beta_0}{\partial\beta_1}\right] \end{aligned} \tag{41}$$

which may be simplified as

$$\begin{aligned} \ln\left(\frac{\beta_2\beta_0}{\beta_1^2}\right) &= \frac{1}{k_B T}\{(U - 2E) - \beta_2 U' - 2\beta_1 E'\} \\ &\equiv -\frac{R}{k_B T} \end{aligned} \tag{42a}$$

or as

$$\beta_2\beta_0/\beta_1^2 = \exp(-R/k_B T) \equiv C \tag{42b}$$

In principle one should now determine $\partial F/\partial\gamma_2 = 0$ and proceed with a complete analysis of the resulting relations. However, in accord with the very limited aim of the present section we skip these more involved steps and merely rationalize the SK equation of state. Namely, we specialize Eqs. (42a) and (42b) to the particular cases considered below:

(i) We set $C = 0$ under the sufficient condition $U \to \infty$. In that event $\beta_2 = 0$ is also a sufficient condition. Eqs. (34a), (36) and (38) may be combined to obtain the free energy of the bond figure assembly as

$$\begin{aligned} [(Z/2)N]^{-1}F_b &= \beta_2 U + 2\beta_1 E + \epsilon_{CA} + k_B T \\ &\times [2\beta_1 \ln \beta_1 + (1 - 2\beta_1)\ln(1 - 2\beta_1)] \end{aligned} \tag{43}$$

It is now useful to introduce the order parameter $\psi \equiv 2\beta_1$. Then

$$\begin{aligned} [(Z/2)N]^{-1}F_b &= \psi E(\psi) + \epsilon_{CA} + k_B T \\ &\times [\psi \ln \psi + (1 - \psi)\ln(1 - \psi) - \psi \ln 2] \end{aligned} \tag{44}$$

When this quantity is optimized via $\partial F_b/\partial\psi = 0$ one obtains

$$\frac{E(\psi) + \psi E'(\psi)}{k_B T} = -\ln\left(\frac{\psi}{1-\psi}\right) + \ln 2 \tag{45}$$

which agrees with the equation of state, Eq. (25), if one introduces the linear form $E = \epsilon\psi - \frac{1}{2}\lambda\psi^2$ and if one sets $g_1 = 2g_0$, as is appropriate to the case at hand. Note that the requirements $U \to \infty$, $\beta_2 \to 0$ converts the three level model of Fig. 12 into a two-level model, with $g_1 = 2$ and $g_0 = 1$, which finally rationalizes the application of the two-state SK theory to the magnetite problem in the first-order regime. Other mani-

festations of the model will be discussed at a later stage.

(ii) We next consider the special case $C = 1$, under the sufficient conditions $U = 2E$ and $U' = E' = 0$. From Eqs. (42b) and (35) one now finds $\beta_2 = \gamma_2^2$, $\beta_1 = \gamma_2(1 - \gamma_2)$, $\beta_0 = (1 - \gamma_2)^2$. Then Eq. (40) simplifies to ($\alpha_1 \equiv \gamma_2$)

$$[(Z/2)N]^{-1}F_b = 2E\alpha_1 + \epsilon_{CA} + 2k_BT[\alpha_1 \ln \alpha_1 + (1 - \alpha_1)\ln(1 - \alpha_1)] \quad (46)$$

which shows that once again the original three level problem has been converted to a quasi-two level problem characterized by the existence of an occupied single site configuration B and an unoccupied single site configuration A, with occupation variables $\alpha_1 \equiv \gamma_2$ and $1 - \alpha_1$. Since there are two sites per bond the free energy of the site assembly is $F_\alpha = \frac{1}{2}F_b$. When the minimization constraint $\partial F_\alpha / \partial \alpha_1 = 0$ is applied, and on introducing the order parameter $\psi = \alpha_1$, one is led to the solution

$$\frac{E(\psi) + \psi E'(\psi)}{k_BT} = -\ln\left(\frac{\psi}{1 - \psi}\right) \quad (47)$$

which reduces to Eq. (25) under the assumption that $E = \epsilon\psi - \frac{1}{2}\lambda\psi^2$ and $g_1 = g_0$. Compared with Eq. (45) the all-important term $\ln 2$ is missing; furthermore, from the mathematical construction it is clear that $g_0 = g_1$ must now hold.

We have thus succeeded in showing that the order–disorder model symbolized by Fig. 12 reduces to the first and second order version of the Strässler–Kittel theory.

As in any thermodynamic theory, the present mean field approach contains parameters (here ϵ, λ, g_1/g_0) that must be determined by fitting theoretical results to the experiment. The procedure adopted for this purpose has been discussed elsewhere in some detail [29], and will not be repeated: basically the ϵ and λ parameters are found by fitting Eq. (33) with $\lambda = 4k_BT_c$ to the linear variation of T_V with δ depicted in Fig. 7. For first order transitions one obtains $\lambda_I = k_B[6.338T_V - 236.1]$, $\epsilon_I = k_B[3.862T_V - 118.0]$ in the range $108 \leq T_V \leq 121$ K, while for second order transitions $\epsilon_{II} = \lambda_{II}/2 = 2k_BT_V$, in the range $82 \leq T_V \leq 101$ K.

Having determined the experimental parameters it is straightforward to find the first order entropy change that occurs at the Verwey transition. Let ψ_l and ψ_u be the lower and upper bounds of ψ for the discontinuity at T_V. Then one finds from Eq. (24) that

$$S_V \equiv S(\psi_u) - S(\psi_l) = Nk_B[(\psi_u - \psi_l)\ln(g_1/g_0) + \psi_l \ln \psi_l - \psi_u \ln \psi_u + (1 - \psi_l)\ln(1 - \psi_l) - (1 - \psi_u)\ln(1 - \psi_u)] \quad (48)$$

Now ψ_u and ψ_l are symmetrically displaced about $\psi = 0.5$. Hence one may introduce Eq. (26) in the above expression to obtain the simple form

$$S_V = Nk_B\kappa \ln(g_1/g_0) \quad (49)$$

It may further be verified that the equation of state for the specific temperature T_V may be rewritten as

$$\frac{\kappa}{2\ln\left(\frac{1 + \kappa}{1 - \kappa}\right)} = \frac{k_BT_V}{\lambda} = \frac{\frac{\epsilon}{\lambda} - \frac{1}{2}}{\ln(g_1/g_0)} \quad (50)$$

Thus, knowing T_V and the corresponding λ value for a given δ, via the parametrization previously described for λ_I, one can obtain κ numerically from Eq. (50) for use in Eq. (49); for first order transitions one sets $g_1/g_0 = 2$. This now yields S_V as a function of δ or of T_V. The calculated curve is shown in Fig. 8, while the experimental values are indicated by the circles. The theory is clearly in very good agreement with experiment; moreover, the fact that $S_V = R\ln 2$ for Fe_3O_4 ($\delta = 0$) readily finds its explanation in the present model.

The striking agreement in the above analysis was achieved because the tiny changes in lattice configuration at the Verwey transition contribute only very little to the total entropy at the first order Verwey transition. The analysis of the second order transition is much less satisfactory. Here one must also determine the total entropy of the lattice as a function of temperature. The electronic contribution $S^e_{II}(T)$ is given by the multiplier of T in Eq. (24) with $g_0 = g_1 = 1$. For a sample with $\delta = 0.012$ and $T_V = 85$ K, ϵ_{II} and λ_{II} can be determined a set forth earlier, and ψ, from Eq. (47). This produces the dashed curve in Fig. 13.

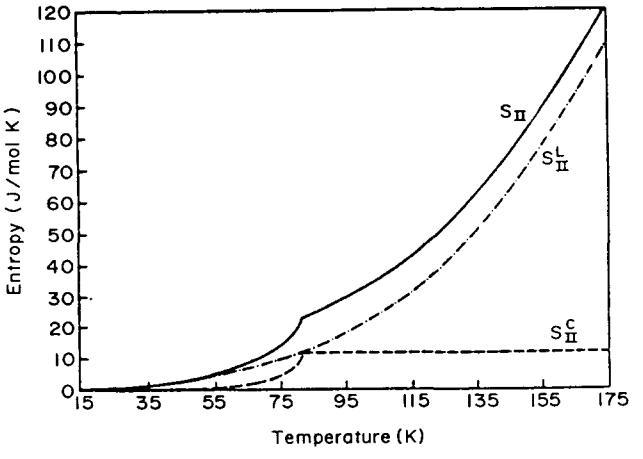

Fig. 13. Calculated variation of the entropy with temperature for a sample undergoing a second order Verwey transition. Dashed curve: $S^e_{II}(T)$ calculated as described in text; note the marked kink at $T_V = 85$ K for a sample with $\delta = 0.012$. Dot–dash curve shows lattice contribution as determined by the Debye model with $\Theta_D = 511$ K. Solid curve represents summation of the two contributions.

We estimate the lattice contribution through the relation $S^{l}_{II}(T) = \psi \int (C_p/T)dT$, where C_p is specified by the Debye equation with $\Theta_D = 511$ K [22]; clearly, this type of calculation furnishes only a crude estimate. The multiplier ψ is introduced because $1 - \psi$ represents that portion of the lattice which is in a frozen configuration. The corresponding calculations is indicated by the dot–dash curve in Fig. 13. The sum $S^{e}_{II}(T) + S^{l}_{II}(T)$, shown by the solid curve, exhibits a noticeable kink near 85 K, the cutoff for the Verwey transition. This calculated quantity may be contrasted with the observed $S(T)$ variation exhibited in Fig. 14. The entropies for samples with $\delta = 0$ (S_I) and $\delta = 0.0121$ (S_{II}) were determined from heat capacity measurements. Not only is the calculated S_{II} curve uniformly too high (a downward adjustment may be achieved by reducing the assumed Θ_D value), but the kink shown in Fig. 13 is notably absent in Fig. 14. Several factors account for the discrepancies. First, as pointed out in Ref. [28], the lattice relaxes significantly as the temperature is raised past T_V. Numerical estimates of one of the optic lattice modes have shown that near T_V there is an anomalous increase in lattice entropy that tends to round off and stretch the kink in S_{II}. This feature has not been taken into consideration. Second, the mean field calculations entirely neglect the fluctuations that become prominent near the transition temperature, as indicated by the experimental heat capacity anomalies. These do not terminate abruptly at T_V, as demanded by mean field theory, but extend considerably above T_V. These fluctuations and/or short-range order effects tend to even out the mean-field discontinuities to such an extent that S^{e}_{II} varies smoothly near T_V. By contrast, such order–parameter fluctuations are intrinsically absent in first order transitions. Until the mean field theory is replaced with an improved version it is difficult to determine whether the present theory can be brought into good accord with the observed second order transitions at T_V.

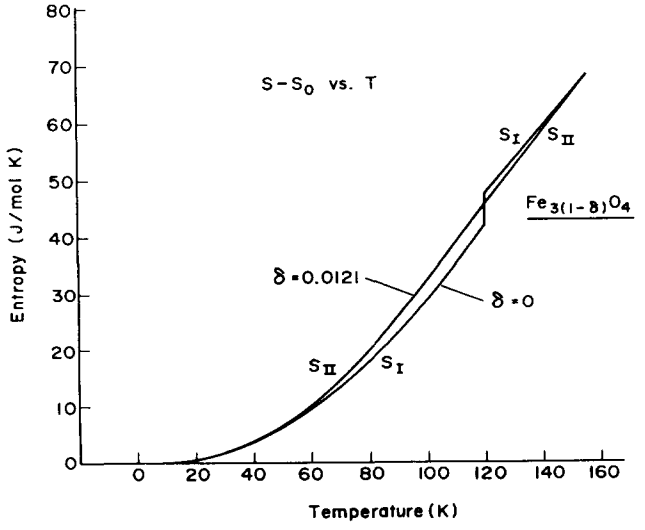

Fig. 14. Observed variation of entropy with temperature as determined from heat capacity measurements on $Fe_{3(1-\delta)}O_4$ for $\delta = 0$ (S_I) and $\delta = 0.0121$ (S_{II}).

8. Electrical characteristics

The order–disorder model should also be able to account for the electrical characteristics of magnetite. We examine below the extent to which this is the case. It has been emphasized by Kloor [25] that one should recognize the existence of $n_p = g_1 N\psi$ quantum resonance states which accommodate polarons at energies ϵ_1; charge carriers that populate these states can respond to an externally applied electric field. There also exist $n_t = g_0 N(1 - \psi)$ trapped states which contain electrons at energies ϵ_0 that are frozen. Since $\psi = \psi(T, \delta)$ these states (and not just the electrons that occupy them) shift in number with temperature. The degree of the occupation of each state at any given T is governed by Fermi-Dirac statistics, such that electron charge balance leads to the expression [29]

$$\frac{1 - 9\delta}{2 - 3\delta} = \frac{g_1\psi}{1 + \exp[-\zeta/k_B T]} + \frac{g_0(1 - \psi)}{1 + \exp[-\zeta - [(\epsilon - \lambda\psi])/k_B T]} \quad (51)$$

where ζ is the Fermi level taken relative to the conducting state. The above expression can be solved analytically for $\zeta(T)$, but it is more convenient to proceed numerically.

In first approximation the Seebeck coefficient for polaron transport is given as [25,29–31]

$$\alpha(T) = -\zeta(T)/qT \quad (52)$$

where q is the magnitude of the electronic charge. Given δ and T, as well as g_1 and g_0, one may obtain ζ from Eq. (51) once ψ is found numerically from Eq. (25) using the ϵ, λ parameterizations described earlier. Then the Seebeck coefficient may readily be evaluated from Eq. (52). The resulting curve for $\delta = 0$ is compared with the experimental results displayed earlier in Fig. 10(b). The agreement between theory and experiment for stoichiometric magnetite is excellent; recall that there has been no adjustment in parameters in moving from thermodynamics to transport parameters.

The resistivity is obtained as the inverse of the conductivity $\sigma = nq\mu$. From an examination of Eq. (51) it is evident that the charge carrier density is specified by

$$n = g_1\psi/[1 + e^{-\zeta/k_B T}] \quad (53)$$

Standard theory [32] shows that in its most elementary

form the mobility for a collection of small polarons is given as

$$\mu = (1-c)qa^2\Gamma/k_B T \tag{54}$$

where a is the separation distance between adjacent octahedral sites. The fraction of empty sites may be read off from the second term in Eq. (51) as

$$1-c = \frac{g_0(1-\psi)}{1+e^{[-(\epsilon-\lambda\psi)-\zeta]/k_B T}} \tag{55}$$

and in rock bottom approximation the jump rate is given by

$$\Gamma = P\nu_0 e^{-E_A/k_B T} \tag{56}$$

Here ν_0 is the appropriate optic phonon frequency that governs the rate of generation of coincidence events between initial and final jump states, E_A is the activation energy for a hopping event, and P is a factor which is unity or one half, depending on whether the jump is adiabatic or not.

The minimum energy for a coincidence event to occur is given by $E_A = |E_p/2| - H$, where E_p is the binding energy of the small polaron and H is the transfer integral. Generally $E_p/2 \gg H$, so that $E_A \approx |E_p/2|$. No strict argument can be provided to determine E_p uniquely, but to first approximation it may be taken equal to $E_A = |E_p/2|\lambda - \epsilon$; ie. to the absolute value of the energy difference $\bar{U} = \epsilon - \lambda\psi$. We now set $\psi = 0$; in this latter case all states are classified as polaron states, and all of these have empty states as target sites. Only after thermally promoting the carrier from the ground to the first excited state is the carrier available for directed drift under an applied electric field. On combining all of the above expressions one obtains

$$\sigma = (2q^2a^2AP\nu_0/k_B T\tilde{V})g_1\psi[1+e^{-\zeta/k_B T}]^{-1}g_0(1-\psi) \times [1+e^{[-(\epsilon-\lambda\psi)-\zeta]/k_B T}]^{-1}e^{-\epsilon/k_B T} \tag{57}$$

In the above, A is Avogadro's number and $\tilde{V}$ is the volume per formula unit. We now set $g_1 = 2g_0 = 2$, determine ϵ and λ as described earlier from empirical fits of T_V vs. δ, set $T = T_V = 121$ K, read off $\psi = \psi(T)$ from Fig. 11, and calculate ζ from Eq. (51). The product $P\nu_0$ is taken to be an adjustable parameter, which through an appropriate optimization routine was found to be roughly 10^{13} and $10^{10}\,s^{-1}$ below and above T_V respectively. The corresponding optical vibration frequencies are in the range deemed appropriate for small polaron transport [33]. A comparison between theory and experiment for the resistivity of stoichiometric magnetite is provided in Fig. 15. Again, there is good agreement between theory and experiment. One must clearly keep in mind, however, that the jump discontinuity in Fig. 15 was fixed by different empirical adjustments of $P\nu_0$ for both the low $T > T_V$ and high $T < T_V$ temperature ranges. Having done this the temperature dependence of $g = 1/\sigma$ is then governed by Eq. (57).

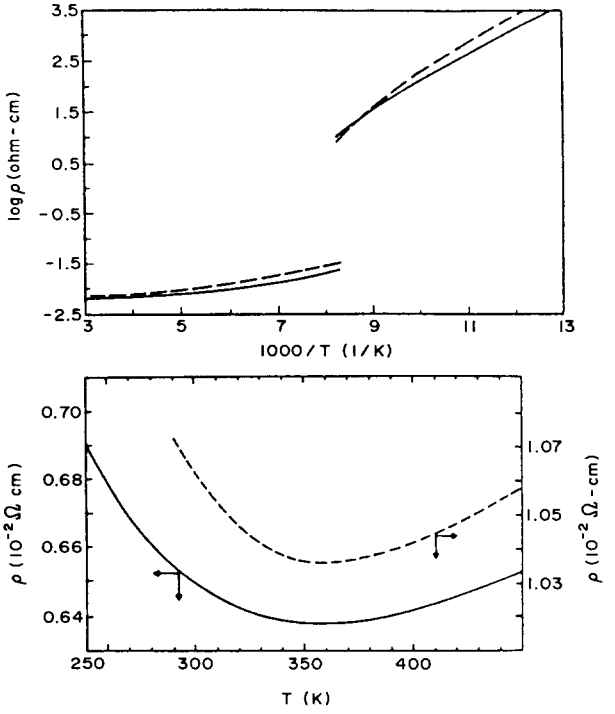

Fig. 15. Comparison of calculated (solid curve) and experimental (dashed curve) variation of resistivity with temperature. The quantity $P\nu_0$ was treated as a free parameter that was adjusted separately for $T < T_V$ and $T > T_V$; see text.

The above analysis shows that the order-disorder model is capable of rationalizing a large body of electrical data; these are consistent with adiabatic small polaron transport of carriers that interact when placed on adjacent octahedral sites. The parametrization used in the analysis of heat capacity data has proven to be applicable in the quantitative verification of conductivity and Seebeck coefficient measurements.

9. Amelioration of the theory

The above approaches toward a theoretical interpretation of the experimental results in magnetite contain several arbitrary features: only selected configurations were included in Table 1; for example, there is no mention of CC, CB, or CA states. Also, Eq. (42) was solved only for two special cases, $C = 1$ and $C = 0$, with quite different dispositions on the energy scale; these were then correlated with first and higher order transitions. In effect, this also involved the assumptions, first that $U \to \infty$ for $\delta < \delta_c$ and second, that $U = 2E$ for $\delta > \delta_c$; it is unreasonable to suppose that slight compositional changes should give rise to such drastic alterations in electron interaction energies.

These unsatisfactory features were recently eliminated in a study by Kloor [25] who initiated a complete and systematic analysis of the entire problem. The only assumption introduced in the systematic construction of the order–disorder formalism was the neglect of all high energy configurations in which two neighboring o-sites are occupied by electrons. This represents a significant departure from the methodology described earlier under the heading of order–disorder theory. One obtains results mathematically essentially identical to those of the present exposition, but the new parameters must be reinterpreted. All of the electrical characteristics can be reproduced by this more systematic approach, using only one free floating parameter. The first and second order aspects were simulated not be adopting two distinct limiting cases, but simply by changes in the parametrization of ϵ and λ in the two regimes. This analysis is now being readied for publication and represents the final improvement in the mean field approach to the Verwey transition in magnetite.

10. Closing remarks

The magnetite system is an interesting proving ground for a wide range of activities in traditional solid state chemistry of transition metal oxides: the synthesis of single crystal specimens, the execution of carefully controlled annealing processes, the measurement of thermodynamic and electrical characteristics (extensive magnetization measurements have not been discussed here), and the construction of a simple model for the interpretation of these findings.

Beyond this analysis, however, it is of interest to the general community that a mean field theory exists which, via a single formalism, can handle both first order and higher order transitions. Lastly, it should be noted that magnetite serves as a reminder that great care must be taken in the control of oxygen stoichiometry in transition metal oxides in order to achieve reproducible experimental results that can be meaningfully subjected to theoretical analysis.

Acknowledgments

The author wishes to express his deep appreciation and gratitude for the very large number of investigators in his laboratory who have been engaged in all phases of the above research effort. Without their dedication and hard work none of the research would have come to fruition. He is singularly indebted to Dr. Ricardo Aragón for his early participation on the project. He is likewise very grateful to Professor J. Spałek of the Jagellonian University, Kraków, Poland, for his penetrating physical insights resulting in an improved description of the Verwey transition. Illuminating discussions with Dr. Harry Kloor are gratefully acknowledged. This research has been supported on NSF grants DMR 86-16533, DMR 92-22986, and INT 93-08323.

References

[1] N.F. Mott, in J. Treusch (ed.), *Festkörperprobleme*, *49* (1979) 331.
[2] N.F. Mott, *Philos. Mag. B*, *42* (1980) 327.
[3] D. Adler, *Solid State Physics*, *21* (1968) 1; *Rev. Mod. Phys.*, *40* (1968) 714.
[4] J.B. Goodenough, *Progr. Solid State Chem.*, *5* (1971) 145.
[5] N.F. Mott, *Metal–Insulator Transitions*, Taylor and Francis, London, 1990, 2nd Edn.
[6] M. Yethiraj and J.M. Honig in T.E. Mallouk (ed.), *Advances in the Synthesis and Reactivity of Solids*, Vol. 2, JAI Press, London, 1994.
[7] R.W. Millar, *J. Amer. Chem. Soc.*, *51* (1929) 215.
[8] E.J.W. Verwey, *Nature*, *144* (1939) 327; E.J.W. Verwey, P.W. Haayman, and F.C. Romeijn, *J. Chem. Phys.*, *15* (1947) 181; E.J.W. Verwey and E.L. Heilmann, *J. Chem. Phys.*, *15* (1947) 174; E.J.W. Verwey and E.L. Heilmann, *Philips Techn. Rev.*, *9* (1947) 185.
[9] H. Flood and D.G. Hill, *Z. Elektrochem.*, *61* (1957) 18.
[10] H. Schmalzried, *Z. Phys. Chem. N. F.*, *31* (1962) 184.
[11] M. Sato, *Geol. Soc. Am. Mem.*, *135* (1972) 189.
[12] H. Kronmüller, R. Schützenauer and F. Walz, *Phys. Stat. Sol., (A)24* (1974) 487; F. Walz, H. Deusch and H. Kronmüller, *Phys. Stat. Sol., (A)53* (1979) 514.
[13] R. Dieckmann and H. Schmalzried, *Ber. Bunsenges.*, *81* (1977) 344; *Ber. Bunsenges.*, *81* (1977) 414; R. Dieckmann, *Ber. Bunsenges.*, *86* (1982) 112.
[14] A.J.M. Kuipers and V.A.M. Brabers, *Phys. Rev. B*, *14* (1976) 1401; *Phys. Rev. B*, *20* (1979) 594.
[15] R. Aragón and R.H. McCallister, *Phys. Chem. Minerals*, *8* (1982) 112.
[16] E. Gmelin, N. Lenge and H. Kronmüller, *Phys. Stat. Sol., (A)79* (1983) 465.
[17] H.R. Harrison, R. Aragón, J.E. Keem, and J.M. Honig, *Inorg. Synth.*, *22* (1984) 43; R. Aragón, H.R. Harrison, R.H. McCallister, and C.J. Sandberg, *J. Cryst. Growth*, *61* (1983) 221; M. Wittenauer, P. Wang, P. Metcalf, Z. Kąkol, J.M. Honig, B.F. Collier and J.F. Greedan, *Inorg. Synth.*, *30* (1995) 124.
[18] See for example Z. Kąkol, J. Sabol and J.M. Honig, *Phys. Rev. B*, *43* (1991) 649.
[19] H.R. Harrison and R. Aragón, *Mater. Res. Bull.*, *13* (1978) 1097; R. Aragón, D.J. Buttrey, J.P. Shepherd and J.M. Honig, *Phys. Rev. B*, *31* (1985) 435.
[20] J. Crank, *The Mathematics of Diffusion*, Clarendon, Oxford, 1975.
[21] J.P. Shepherd, J.W. Koenitzer, R. Aragón, C.J. Sandberg and J.M. Honig, *Phys. Rev. B*, *31* (1985) 1107; J.P. Shepherd, J.W. Koenitzer, C.J. Sandberg, R. Aragón and J.M. Honig, *J. Mol. Cryst. Liq. Cryst.*, *107* (1984) 191; J.P. Shepherd, R. Aragón, J.W. Koenitzer and J.M. Honig *Phys. Rev. B*, *32* (1985) 1818; J.P. Shepherd, J.W. Koenitzer, R. Aragón, J. Spałek and J.M. Honig, *Phys. Rev. B 43* (1991) 8461.
[22] J.W. Koenitzer, P.H. Keesom and J.M. Honig, *Phys. Rev. B*, *39* (1989) 6231.
[23] J.M. Honig, *J. Solid State Chem.*, *45*, (1982) 1.

[24] P. Wang, Z. Kąkol, M. Wittenauer and J.M. Honig, *Phys. Rev. B*, *42* (1990) 4553; A. Kozłowski, R.J. Rasmussen, J. Sabol, P. Metcalf and J.M. Honig, *Phys. Rev. B*, *48* (1993) 2057.
[25] H. Kloor, Ph. D. Thesis, Purdue University, 1994, unpublished.
[25a] R. Aragón and J.W. Koenitzer, *J. Solid State Chem.*, *113* (1994) 225.
[26] R. Aragón, D.J. Buttrey, J.P. Shepherd and J.M. Honig, *Phys. Rev. B*, *31* (1985) 430; R. Aragón, J.P. Shepherd, J.W. Koenitzer, D.J. Buttrey, R.J. Rasmussen and J.M. Honig, *J. Appl. Phys.*, *57* (1985) 3222.
[27] S. Strässler and C. Kittel, *Phys. Rev.*, *139* (1965) *A*758.
[28] J.M. Honig and J. Spałek, *J. Less-Common Metals*, *156* (1989) 423; J.M. Honig, J. Spałek and P. Gopalan, *J. Amer. Ceram. Soc.*, *73* (1990) 3225; J.M. Honig and J. Spałek, *J. Solid State Chem.*, *96* (1992) 115.
[29] R. Aragón and J.M. Honig, *Phys. Rev. B*, *37* (1988) 209; J.M. Honig, *Phys. Chem. Minerals*, *15* (1988) 476.
[30] D. Kim and J.M. Honig, *Phys. Rev. B*, *49* (1994) 4438.
[31] D. Emin, *Phys. Rev. B*, *20* (1984) 5766.
[32] See for example J.M. Honig, *J. Chem. Ed.*, *43* (1966) 76; H.L. Tuller and A.S. Nowick, *J. Phys. Chem. Solids.*, *38* (1977) 859.
[33] T. Holstein, *Ann. Phys. (NY)*, *8* (1959) 325, 343; I.G. Austin and N.F. Mott, *Science*, *168* (1970) 70.